The retrieval of warm rain from CloudSat

Matthew D. Lebsock[1] and Tristan S. L'Ecuyer[1]

Received 6 April 2011; revised 7 July 2011; accepted 11 August 2011; published 26 October 2011.

[1] An algorithm for the retrieval of warm rain over oceans for CloudSat that uses ancillary information from the Moderate Resolution Imaging Spectroradiometer (MODIS) instrument is presented. The method builds upon the architecture of the standard CloudSat 2C-RAIN-PROFILE product. Several general enhancements of that architecture have been made, including the implementation of a fast two-stream multiple-scattering radar model and a detailed error characterization. The algorithm has also been modified to specifically target the retrieval of warm rain by using ancillary MODIS visible optical depth observations to construct a parameterization of the cloud water path, implementing a model of the evaporation of rain below cloud base, and introducing a realistic representation of warm raindrop size distributions. With these important algorithm modifications, the CloudSat 2C-RAIN-PROFILE product is ideally suited to examine the distribution and magnitude of light rain over oceans.

Citation: Lebsock, M. D., and T. S. L'Ecuyer (2011), The retrieval of warm rain from CloudSat, *J. Geophys. Res.*, *116*, D20209, doi:10.1029/2011JD016076.

1. Introduction

[2] The prevalence of warm rain over the oceans has been well known for some time [e.g., *Battan and Braham*, 1956], however much of this rain is modest in intensity and as a result conventional satellite-based remote sensing methods have little skill in identifying its occurrence let alone quantifying its intensity. Through a comprehensive analysis of shipboard weather reports, *Petty* [1995] showed that the dominant modes of precipitation are drizzle and transient showers in expansive areas of the subtropical oceans. He points out that these modes of precipitation represent significant challenges to spaceborne precipitation methodologies based on visible, infrared (IR), or passive microwave observations. Historically, infrared [*Arkin*, 1979] or merged visible-IR methods [*Lovejoy and Austin*, 1979] attempted to quantify precipitation using simple brightness temperature thresholds that were statistically tuned to produce a reasonable precipitation climatology. The physical motivation behind such an approach was that cold high clouds would be associated with the heaviest rain. However, these methods have little skill at identifying warm precipitation where the infrared brightness temperatures fall above the precipitation thresholds. More physically grounded rainfall algorithms use passive microwave (PMW) observations that are directly sensitive to the bulk emission from liquid water as well as the scattering of high-frequency microwave radiation by lofted ice [*Wilheit*, 1986]. However, in the case of warm precipitation where an ice- scattering signal is absent, any PMW method will suffer an inherent ambiguity in distinguishing nonprecipitating cloud from precipitation [*Stephens and Kummerow*, 2007]. Even if rainfall could be identified unambiguously, microwave algorithms still need to partition the observed emission signal between cloud and rainwater, which are often of the same order of magnitude for warm rain [*Lebsock et al.*, 2011] leading to a further ambiguity in quantifying the rain intensity.

[3] The Tropical Rainfall Measurement Mission (TRMM) precipitation radar (PR) makes the most direct observation of precipitation from space and offers the current benchmark in terms of global precipitation measurements. The radar reflectivity observed by this sensor is insensitive to the presence of cloud water and therefore does not suffer the ambiguities associated with PMW techniques. However, the PR has a minimum detectable signal of 17 dBZ, which limits its ability to observe the light end of the rainfall intensity distribution. The PR may miss light rain composed of low concentrations of small raindrops that produce weak reflectivity signatures, echo top heights that are shallow enough to be obscured by the radar surface return, or due to partial beam filling of the 5 km PR footprint by isolated showers. *Schumacher and Houze* [2000] estimate that the PR misses 2.3% of the rainfall accumulation near the Kwajelin Atoll due to some combination of these factors, however there is good reason to suspect that this rather optimistic regional result may not be applicable to all oceanic regimes. For example, *Short and Nakamura* [2000] develop a statistical model of the PR echo top heights and radar reflectivity distributions that suggests that the PR misses as much as 20% of the shallow rain in the tropics and *Berg et al.* [2010] use collocated PR and CloudSat observations to estimate that the PR misses 10% of the total rainfall accumulation in the tropical and subtropical oceans. Furthermore, the most recent version of the Goddard precipitation profiling algorithm [*Kummerow et al.*, 2011] uses a methodology that merges passive microwave observations with PR observations in a manner

[1]Department of Atmospheric Science, Colorado State University, Fort Collins, Colorado, USA.

0148-0227/11/2011JD016076

that is physically consistent with both sensors to develop a rainfall database. This new database increases rain rates by 4.2% over the PR solution and much of this difference results from the addition of light rain that falls below the minimum detectable signal of the PR.

[4] Because of the inherent difficulty of conventional remote sensing methods to identify the occurrence and quantify the intensity of warm rain there has been increased interest in the use of the CloudSat millimeter wave Cloud Profiling Radar (CPR) observations to observe warm rain. For example, *Lebsock et al.* [2008] estimate that 6.5% of warm clouds over oceans precipitate, *Chen et al.* [2011] estimate that warm rain accounts for 31.2% of all rain events, and *Leon et al.* [2008] use a simple reflectivity-rain rate (Z-R) relationship to assign drizzle rates based on the maximum reflectivity observed in warm clouds. Application of a simple Z-R relationship to CloudSat data to estimate the surface rain rate is complicated by two factors. First, because of the 94 GHz operating frequency of the CPR, attenuation by both gasses and hydrometeors cause the observed reflectivity (Z) to appear smaller than the unattenuated single scatter reflectivity (Z_{ss}). This effect compounds along the radar path reaching a maximum at the Earth's surface. One would ideally like to relate the observed reflectivity in the range gate closest to the surface directly to the surface rain rate however the presence of attenuation above this gate necessitates an attenuation correction procedure. It is well known [*Hitschfeld and Bordan*, 1954] that this approach can result in catastrophic errors for heavily attenuating frequencies like that of the CPR. An additional inconvenience is the presence of multiple-scattering effects that alias the scattering signal from one range gate into range gates further from the radar system. Both the attenuation correction and the multiple-scattering signal thus build from the top down maximizing at the Earth's surface and complicate the relationship between the observed near-surface reflectivity and rain rate. Attenuation decreases the apparent reflectivity whereas multiple scattering increases the apparent reflectivity with attenuation effects tending to dominate. Even in light and moderate rain these effects must be accounted for and can completely obscure the relationships between the radar reflectivities and rain rate in heavy rain [*Battaglia et al.*, 2008]. Fortunately, attenuation and multiple-scattering effects are minimized in shallow, light precipitation, precisely the types of rain events where conventional sensors struggle and CloudSat has the most to contribute to the global rainfall climatology. An additional and fundamental limitation of CloudSat as a precipitation sensor is that it suffers from surface clutter contamination in the first two radar bins above the surface over ocean and the first three bins over land. As a result surface precipitation must be inferred from the reflectivity in the lowest clutter-free bin leading to unavoidable errors in estimating the amount of precipitation that evaporates between this elevated layer and the surface.

[5] *L'Ecuyer and Stephens* [2002] introduce an optimal estimation (OE) framework to retrieve rain profiles using CloudSat reflectivity profiles in conjunction with an integral constraint on the path-integrated attenuation (PIA). The key element of this work is a recasting of the "noise" in the attenuation from precipitation water as a "signal" through the use of an integral constraint on the solution. This approach has a heritage in the PR retrieval algorithm [*Iguchi et al.*, 2000], which also employs a PIA constraint on the derived rain rates. *Haynes et al.* [2009] outline a method specific to the CPR to derive the PIA that employs an empirical relationship between the clear sky surface backscattering cross section and the 10 m wind speed and sea surface temperature. They further develop a simple algorithm for using the PIA to infer surface rain rate, which assumes that the rainfall is vertically invariant. *Matrosov* [2007] uses an alternative attenuation-based technique in which the vertical gradient of reflectivity is used in conjunction with the assumption of a vertically uniform rain column to deduce the attenuation and relate this to surface rain rate. Both of these attenuation techniques are useful for moderate to heavy precipitation, however they have little applicability to the warm rain problem where significant vertical variation exists in the structure of rainfall and the attenuation signal is often smaller than the noise inherent in the PIA observation. *Mitrescu et al.* [2010] present a preliminary application of the OE framework utilizing both the reflectivity profile and a PIA constraint in introducing the operational CloudSat 2C-RAIN-PROFILE product, however the algorithm assumptions made in that work are not particularly well suited to the retrieval of warm rain. In particular the attenuating effect of cloud water is not modeled and the assumed precipitation drop size distribution is not appropriate for warm rain. Additional and more general deficiencies of early versions of 2C-RAIN-PROFILE include the lack of a multiple-scattering model and simplistic error characterization that neglects the error introduced through physical assumptions.

[6] To address some of the known shortcomings of the early versions of the 2C-RAIN-PROFILE product, this paper presents a multisensor A-Train algorithm specific to oceanic warm rainfall that builds upon the previously mentioned studies. Following *L'Ecuyer and Stephens* [2002] the method uses both the full reflectivity profile and an integral attenuation constraint. Elements of this paper that differentiate it from previous research include (1) the use of visible optical depth measurements to provide a constraint on the cloud component of the water path (W_c), (2) an improved error characterization, (3) modeling of precipitation optical properties using drop size distributions (DSDs) appropriate for warm rain, (4) inclusion of a model of subcloud evaporation, and (5) the implementation of a physical model of multiple scattering to correct both the reflectivity profile and the PIA. The algorithm presented here is research oriented, however the new elements of this work form the basis for ongoing upgrades to the operational CloudSat rainfall products.

2. Data

[7] Data from release 04 of the standard CloudSat data products and the Moderate Resolution Imaging Spectroradiometer (MODIS) MOD06 (version 5.1) cloud product [*Platnick et al.*, 2003] for the year 2007 were used in this study.

[8] The first step in the data reduction was to identify raining pixels, which were found using the rain flag in the 2C-PRECIP-COLUMN product [*Haynes et al.*, 2009]. That product has four categories describing the likelihood of surface precipitation ranging from nonraining to rain certain. Intermediate categories are associated with near-surface reflectivities less than 0 dBZ that are most likely associated

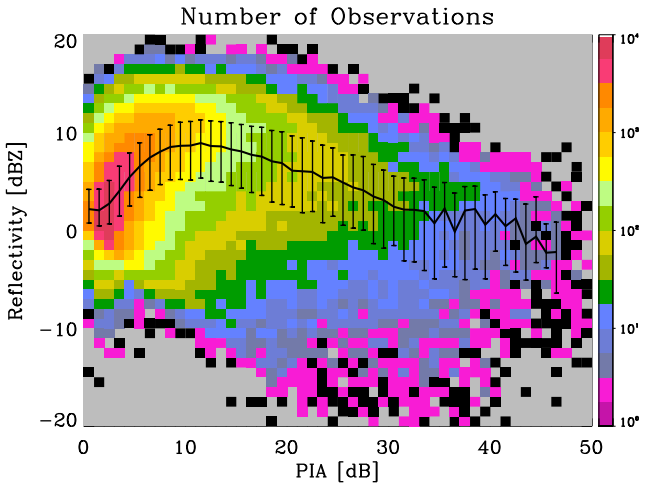

Figure 1. The joint histogram of the apparent PIA and the near-surface reflectivity. No corrections for attenuation or multiple scattering have been made.

with drizzle and light rain that does not reach the surface. For this reason the results presented here are limited to cases that are identified as rain certain. After identifying raining pixels, warm rain was discriminated from ice phase rain using the CPR Echo Top flag contained in the 2B-GEOPROF product. The remaining raining pixels have cloud top pressures greater than 500 hPa and cloud top temperatures warmer than 273 K according to the European Centre for Medium-Range Weather Forecasts (ECMWF)–AUX product, which contains ECMWF analysis fields that are spatio-temporally interpolated to the CloudSat radar bins.

[9] Once the warm raining pixels were identified, profiles of radar reflectivity (Z), gaseous attenuation, and a hydrometeor mask are taken from the 2B-GEOPROF product [*Marchand et al.*, 2008]. The hydrometeor mask is composed of a flag ranging in value from 0 through 40 with increasing values corresponding to increasing likelihood of cloud. A conservative threshold of 30, which has a false detection goal of 2% [*Marchand et al.*, 2008], was used to discriminate cloudy from clear bins since the focus is on precipitation and not tenuous cloud layers. The ECMWF-AUX product provides corresponding profiles of temperature, pressure and humidity that are linearly interpolated in time and space to the CPR radar volume. In addition to the reflectivity profiles, two integral constraints were employed in the retrieval algorithm. The first is an estimate of the PIA, which was taken from 2C-PRECIP-COLUMN. The second is an observation of the visible optical depth (τ) from MODIS, which provides an independent integral constraint on the cloud water path (W_C).

3. Algorithm Description

3.1. Scope of the Problem

[10] The intent of this paper is to outline a methodology for deriving profiles of precipitation water content (l_p) while simultaneously constraining the cloud water path in an effort to estimate the surface rainfall (R) using observations from CloudSat and MODIS. Specifically, a given radar profile with N cloudy bins has $N + 2$ observations, including a vector of reflectivities $\mathbf{Z} = [Z_1, \ldots Z_N]$, the PIA and $\log_{10}(\tau)$. From these observations, a "state" vector, $\mathbf{x} = \log_{10}[l_1, \ldots, l_N, W_C]$, composed of $N + 1$ parameters will be retrieved. To improve the linearity in the radiative model that maps the state parameters into the observations the logarithmic transform is used while the conventional decibel units are used for Z and PIA. The desired goal of estimating the surface rain rate is achieved by assuming a relationship between the precipitation liquid water content in the lowest resolvable radar bin (l_N) and the surface rain rate.

[11] The physical basis for such an approach is that the radar reflectivities are primarily a function of the precipitation water content, whereas the optical depth is most sensitive to the cloud water path, and the PIA is a function of both cloud and precipitation water. The two integral constraints (PIA, τ) thus act to constrain both the total water path and partition water between the cloud and precipitation modes while the vertical distribution of precipitation water is determined by the reflectivity profile. The independent optical depth constraint on the cloud water path is helpful when observing light precipitation with the CPR because the radar reflectivities are insensitive to the cloud water in the presence of rain however cloud water can have measurable effect on the attenuation of the radar beam.

[12] A key element of this work centers on designing a retrieval of R that transitions from a reflectivity-based retrieval for light rain when the attenuation is small to an attenuation-based retrieval at high rain rates when the attenuation is large. In this work, use of the subjective term high rain rates is tied to this transition from reflectivity to attenuation and is roughly given by 2–3 mm h^{-1}. The need for such a transition in the retrieval framework is highlighted in Figure 1, which shows a joint histogram of the PIA and the near-surface reflectivity observations for the retrievals presented in this paper. A nonmonotonic relationship is observed between the PIA and the near-surface reflectivity with reflectivity initially increasing with PIA and then decreasing as PIA becomes large. It is extremely difficult to assign rainfall intensity estimates to these heavily attenuated reflectivities due to the propagation of errors discussed by *Hitschfeld and Bordan* [1954], thus highlighting the importance of PIA as a signal that can be exploited in heavy rain.

3.2. Radiative Model

[13] Simulated radar reflectivites (Z_{sim}) and path-integrated attenuation (PIA_{sim}) are calculated from Mie scattering theory using the general expressions,

$$\begin{aligned} Z_{sim} &= Z_{ss} + \Gamma_{ms} - \Gamma_{att} \\ \mathrm{PIA}_{sim} &= \mathrm{PIA}_{ss} - \Gamma_{ms} \end{aligned}, \qquad (1)$$

where Γ_{ms} represents a multiple-scattering correction and Γ_{att} represents an attenuation correction both of which are defined to be greater than 0. Attenuation effects tend to dominate the correction to the single-scattering reflectivity with attenuation by water vapor regularly exceeding 6 dB in the tropics and attenuation in heavy precipitation exceeding 100 dB. Multiple-scattering effects are generally small in warm rain but they are often not negligible in shallow cumulus showers when rain rates become moderate in intensity. It is critical to account for these effects because in many regions much of the total accumulation from warm rain derives from these

moderate to heavy rain events. In this work multiple scattering is modeled using the fast time-dependent two-stream (TDTS) method of *Hogan and Battaglia* [2008]. The TDTS model has been shown to compare favorably with benchmark Monte Carlo simulations while being significantly more computationally efficient. Furthermore, any inverse application of a multiple-scattering model will be far more sensitive to the necessary assumption of a precipitation DSD than to the precision of the model itself, which discourages the use of a more complex model. Here, the TDTS model is used to correct both the reflectivities and the observed PIA for multiple-scattering effects. Multiple scattering always increases the apparent reflectivity therefore these corrections always reduce the single-scattering reflectivity values while increasing the PIA estimate.

[14] The visible optical depth is approximated from both the cloud and precipitation water contents,

$$\tau_{sim} = \frac{3Q_{ext}}{4\rho_l} \int_{z=0}^{H} \left(\frac{l_c}{r_{e,c}} + \frac{l_p}{r_{e,p}} \right) dz, \tag{2}$$

where ρ_l is the density of water, the integral is calculated from the ocean surface to cloud top (H), and it has been approximated that the extinction efficiency (Q_{ext}) = 2 [*Stephens*, 1978]. Uncertainty introduced by this approximation is small relative to the uncertainty in the observed optical depth, which for precipitating clouds is at least 20% based on instrument noise [*Nakajima and King*, 1990] and the assumption of $r_{e,c}$. Because of the inverse relationship with r_e, cloud water dominates the optical depth, however the precipitation mode water plays a nonnegligible role when the precipitation is composed of relatively small drizzle drops. Depending on the details of the DSD, the influence of precipitation mode water on the visible optical depth may be as large as 5–10% [*Lebsock et al.*, 2011].

3.3. Retrieval Framework

[15] The retrieval framework follows the OE methodology that has been described in detail elsewhere [*L'Ecuyer and Stephens*, 2002] but a brief review is provided here for completeness. The retrieval seeks to minimize the cost function,

$$\Phi = [\mathbf{Z_{sim}} - \mathbf{Z}]^{\mathbf{T}} \mathbf{S_z} [\mathbf{Z_{sim}} - \mathbf{Z}] + [\mathbf{x} - \mathbf{x_a}]^{\mathbf{T}} \mathbf{S_a} [\mathbf{x} - \mathbf{x_a}] + \frac{(\mathrm{PIA}_{sim} - \mathrm{PIA})^2}{\sigma^{\sigma}_{\mathrm{PIA}}} + \frac{(\tau_{sim} - \tau)^2}{\sigma^2_{\tau}}, \tag{3}$$

where $\mathbf{x_a}$ represents an a priori estimate of the state ($\mathbf{x}$), $\mathbf{Z}$ represents a vector containing the reflectivity profile, PIA represents the path-integrated attenuation, τ represents the visible optical depth, the subscript *sim* denotes a simulated quantity, $\mathbf{S_z}$ is the observation error covariance matrix, $\mathbf{S_a}$ is the a priori error covariance matrix, and σ^2 represents the estimated error variance in PIA and τ. The error variances and covariances determine the relative influence of the four terms in determining the retrieved state. The cost function is minimized in a straightforward manner using Newtonian iteration until a solution is achieved that provides an optimal match to both the observations and a priori constraints given their relative error bounds. The value of the cost function (Φ) at convergence represents a measure of the goodness of fit between the physical model and the observations and should approximately follow a χ^2 distribution with $N + 2$ degrees of freedom. It is useful to define a maximum allowable χ^2 threshold value above which retrievals are flagged as suspect.

[16] With the assumption of Gaussian statistics some useful error diagnostics may be defined from equation (3) including a retrieval error covariance matrix,

$$\mathbf{S_x} = \left[\mathbf{S_a^{-1}} + \mathbf{K^T S_z^{-1} K} + \frac{\mathbf{L^T L}}{\sigma^2_{\mathrm{PIA}}} + \frac{\mathbf{M^T M}}{\sigma^2_{\tau}} \right], \tag{4}$$

where $\mathbf{K} = \partial \mathbf{Z}_{sim}/\partial \mathbf{x}$, $\mathbf{L} = \partial \mathrm{PIA}_{sim}/\partial \mathbf{x}$, and $\mathbf{M} = \partial \tau_{sim}/\partial \mathbf{x}$ are kernel weighting functions representing the sensitivity of the simulated observation to the retrieval parameters. The diagonal elements of $\mathbf{S_x}$ are the retrieval error variances corresponding to each of the retrieved parameters in $\mathbf{x}$. Following *L'Ecuyer and Stephens* [2002], the total retrieval error covariance matrix may be broken down into contribution matrices,

$$\mathbf{S_x} = \mathbf{C}_Z + \mathbf{C_a} + \mathbf{C}_\tau + \mathbf{C}_{\mathrm{PIA}}, \tag{5}$$

where the matrices on the right-hand side correspond to the component of retrieval error deriving from the reflectivity profile the a priori constraint, the visible optical depth constraint, and the PIA constraint, respectively. The ratio of any diagonal element of a contribution matrix ($\mathbf{C}$) to the corresponding element of the retrieval error covariance matrix ($\mathbf{S_x}$) provides a measure of the fractional contribution of that constraint to the derived solution for that particular element of $\mathbf{x}$. For example, to determine the fractional contribution of the PIA constraint to the derived near-surface rain rate given in element $\mathbf{x}_N$ of the state vector one would calculate $\mathbf{C}_{\mathrm{PIA},NN}/\mathbf{S}_{\mathbf{x},NN}$ which would vary between 0 when the PIA does not contribute and 1 when the PIA fully determines the answer.

3.4. Microphysical Algorithm Assumptions

[17] The problem of estimating the rain rate from the observations is incompletely defined as posed and requires a number of simplifying assumptions. These assumptions take the form of simple physical models that are imposed upon the problem to make the necessary radiative calculations possible. These models include (1) a model to distribute cloud water in the vertical and determine the cloud DSD, (2) a model of evaporation of rain below cloud base, and (3) a model of the precipitation DSD. Descriptions of these models are described in section 3.4.1.

3.4.1. Cloud Model

[18] A linearly stratified cloud model is assumed in which cloud water content increases linearly with height from cloud base to cloud top and cloud effective radius (r_e) increases to the one-third power above cloud base [*Bennartz*, 2007]. A cloud top effective radius of 15 μm is assumed. MODIS effective radii could also be used to assign the cloud top radius, however these products are not used in this work due to difficulties in their interpretation due to penetration depth [*Platnick*, 2000] and three-dimensional radiative [*Marshak et al.*, 2006] effects. Cloud water is distributed from the first cloudy bin at the top of the profile to the lowest resolvable bin, which varies by ±120 m around a height of ~720 m. An assumption regarding the height of cloud base is neces-

Table 1. The Parameters of the Warm Rain Reflectivity-Rain Rate (Z-R) Relationships of the Form $Z = aR^{b}$[a]

Cloud Type	a	b	α	β
Nimbostratus	25.0	1.3	1.751	0.223
Congestus	88.0	1.5	2.179	0.335

[a] Z is in mm^6/m^3 and R is in mm/h. These relationships are used to derive a parameterization of the DSD of the form, $\lambda^{-1} = \alpha l_p^{\beta}$, where λ is the slope parameter of the truncated exponential size distribution in μm^{-1} and l_p is the precipitation liquid water content in g/m^3.

sary because no observation of cloud base is possible in rain. Another possible choice for cloud base could be the lifting condensation level calculated from the ECMWF model analysis fields, which is on average approximately 200 m lower than the lowest resolvable radar bin. Retrieval results are not particularly sensitive to this assumption because the cloud water content is small at cloud base. The linearly stratified cloud model with the stated assumptions fully describes both the microphysical (DSD) and the vertical distribution of cloud water.

3.4.2. Evaporation Model

[19] Rainwater is distributed from the first cloudy bin at the top of the profile to the ocean surface. The vertical distribution of this water is to be determined by the measurements. A simple model derived for nimbostratus is used to model evaporation below cloud base [*Comstock et al.*, 2004],

$$R(z) = R_{CB} e^{-k\chi\left(\bar{r}_p, z\right)}$$
$$\chi = \left[\frac{(z_{CB} - z)}{\bar{r}_p^{2.5}}\right] \quad , \tag{6}$$

where $R(z)$ is the rain rate at some height (z) below cloud base, R_{CB} is the cloud base rain rate, $\bar{r}_p$ is the mean radius of the precipitation drop size distribution, and $k = 320$ [μm$^{3.75}$ m$^{-1.5}$]. While this model is somewhat simplistic it has the desired effect of significantly evaporating light drizzle falling from cloud base to the surface while having a modest effect on moderate to heavy rain because of the strong dependence on the mean radius of the size distribution.

3.4.3. Raindrop Size Distributions

[20] By far the most troubling assumption that must be made in any radar rainfall algorithm is that of the rain DSD. Because the focus of the this work is on light precipitation in which the precipitation drops are often only a few times larger than the cloud droplets a truncated exponential distribution is used to model the DSD,

$$n(r) = \frac{N_p}{\bar{r}_p - r_o} \exp\left[-\left(\frac{r - r_o}{\bar{r}_p - r_o}\right)\right], \tag{7}$$

where N_p is the precipitation number concentration and r_o is the truncation radius, which is assigned a value of 25 μm. The moments of the truncated exponential distribution are given by,

$$M_i = \int_{r=r_o}^{\infty} r^i n(r) dr = N_p \frac{i!}{\lambda^i} \sum_{j=0}^{i} \frac{(r_o\lambda)^j}{j!}. \tag{8}$$

This expression provides the effective radius as $r_e = M_3/M_2$ and the precipitation liquid water content as $l_p = (4/3)\pi\rho_l M_3$. The DSD may be simplified by setting $\lambda = 1/(\bar{r}_p - r_o)$and $N_o = N_p\lambda$ to give $n(r) = N_o \exp[-\lambda(r - r_o)]$ where N_o and λ are known as the intercept and slope parameters, respectively. In the well-known formulation of *Marshall and Palmer* [1948], r_o is implicitly set to 0 and N_o is set to a constant value so that variations in the drop number concentration are perfectly correlated to variations in the mean radius of the distribution.

[21] Previous versions of the 2C-RAIN-PROFILE algorithm have adopted a universal Marshall-Palmer size distribution that is generally inappropriate for warm rain. For example, *Comstock et al.* [2004] show that for drizzling stratocumulus, variation in the precipitation rate is best explained through variations in the droplet number concentration and that the assumption of a constant intercept parameter is not appropriate. In the present work two different Z-R relationships are chosen represent the warm rain DSDs. The first is applicable to nimbostratus [*Comstock et al.*, 2004] and the second is applicable to cumulus congestus [*Snodgrass et al.*, 2009].

[22] The Z-R expressions relate radar reflectivity to rain rate, however they do not provide the other optical properties, in particular the volume extinction coefficient that is necessary to simulate a profile of radar reflectivities. To this end, a method to parameterize the DSD from any Z-R relationship is developed. First values of N_p and $\bar{r}_p$ are derived that match the Z-R relationship along the range of reflectivities varying from −20 to 10 dBZ where the fall velocity observations of *Gunn and Kinzer* [1949] are used to relate the size distribution to a specific rain rate. From the derived values of N_p and $\bar{r}_p$ a parameterization of the DSD is found by fitting a relationship between the slope parameter and the liquid water content of the form $\ln(\lambda^{-1}) = \ln(\alpha) + \beta\ln(l_p)$ using ordinary linear regression. This relationship can be more compactly expressed as $\lambda^{-1} = \alpha l_p^{\beta}$ and completely defines the DSD parameterization subject to the previously mentioned size distribution truncation given by r_o. For example, N_p may be found by invoking the definition of the liquid water content and the expression for the moments of the DSD provided above. Once N_p and λ have been determined any radiative property at any frequency may be calculated. Table 1 provides the coefficients of the Z-R relationships and of the DSD parameterizations for both the drizzle and cumulus DSDs.

[23] Figure 2 shows physical and optical parameters of the drizzle, cumulus, and Marshall-Palmer DSDs. The most important difference seen in Figure 2 is that for a given rain rate the drizzle DSD contains substantially more water and has much higher number concentrations than the cumulus or the Marshall-Palmer distribution. It follows that the drizzle DSD is associated with smaller reflectivities and larger attenuation than the cumulus and Marshall-Palmer DSDs because reflectivity is a strong function of drop size whereas attenuation is a strong function of water mass.

[24] To determine which DSD to assume for any given pixel a cloud top height threshold of 2 km is chosen to transition from the drizzle to the cumulus DSD. Figure 3 shows the geographical distribution of the fraction of warm raining clouds that have observable radar echo tops higher than 2 km according to the GEOPROF product. Warm rain with echo tops below 2 km is most frequent in the subtropical subsidence regions and the midlatitudes whereas deeper warm rain

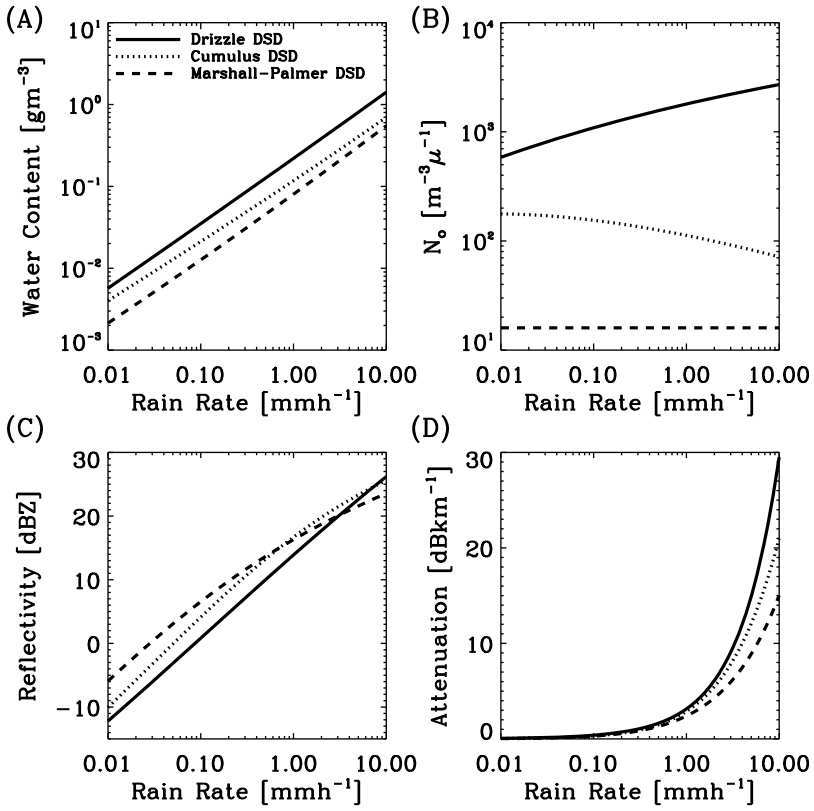

Figure 2. Some key microphysical and optical parameters of the drop size distributions examined in the paper.

clouds occupy the large majority of the tropical oceans, thus providing some qualitative justification for the 2 km threshold. This threshold is admittedly ad hoc, however it does have the desired effect of providing regional variation in the assumed drop size distribution that imposes regional variation in the retrieved rain rates.

3.5. Error Covariance Matrices

[25] The true utility of the OE retrieval framework lies in careful error characterization, the details of which are buried in the process of defining the elements of the $\mathbf{S_z}$ and $\mathbf{S_a}$ error covariance matrices. To begin the discussion of the error covariance, it is noted that the diagonal elements of these matrices represent variances such that $\mathbf{S}_{ii} = \sigma_{ii}^2$, whereas the off-diagonal elements represent covariances such that $\mathbf{S}_{ij} = \rho_{ij}\sigma_{ii}\sigma_{jj}$, where ρ_{ij} is the correlation between the uncertainties. Our previous applications of the OE framework to the CloudSat precipitation retrieval problem have considered $\mathbf{S_a}$ and $\mathbf{S_z}$ to be diagonal matrices with constant variance values that did not change during the retrieval iteration or even from one pixel to the next. In reality, errors are often correlated and the values that compose the $\mathbf{S_a}$ and $\mathbf{S_z}$ matrices should vary with the estimated state ($\mathbf{x}$). To this end, a detailed outline for a more complete characterization of the error characterization follows beginning with the a priori error covariance ($\mathbf{S_a}$) and followed by the measurement error covariance ($\mathbf{S_z}$).

[26] Because rain and cloud water contents vary by orders of magnitude on scales less than the sampling volume of the radar, there can be no real a priori knowledge of the magnitude of the state prior to observation. Nonetheless the inclusion of the a priori term does allow for certain physical constraints to be imposed on the retrieved state. For example, it is known a priori that because rain falls through the atmospheric column that the precipitation at one height level will be correlated with the precipitation at adjacent levels. Therefore in this work the a priori term is used not to constrain the magnitude but rather to impose these correlations, thus acting as a smoothing constraint on the minimization. First, the diagonal elements of $\mathbf{S_a}$ are set to very large values ($\sigma_{a,ii}$ covers ± 3 orders of magnitude) covering the entire range of possible rainwater contents. Second, the magnitude of the

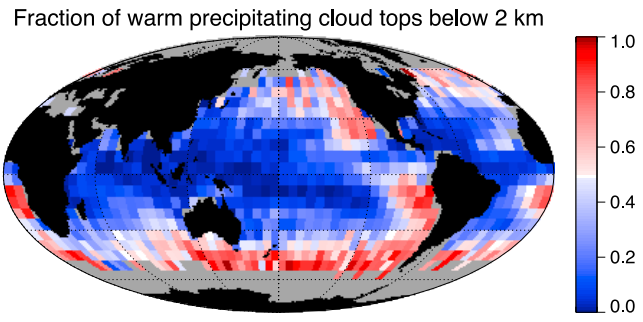

Figure 3. Fraction of warm rain ($T_b > 273$ K) clouds with cloud tops below 2 km. This is the height threshold chosen to transition from a drizzle drop size distribution to a cumulus drop size distribution.

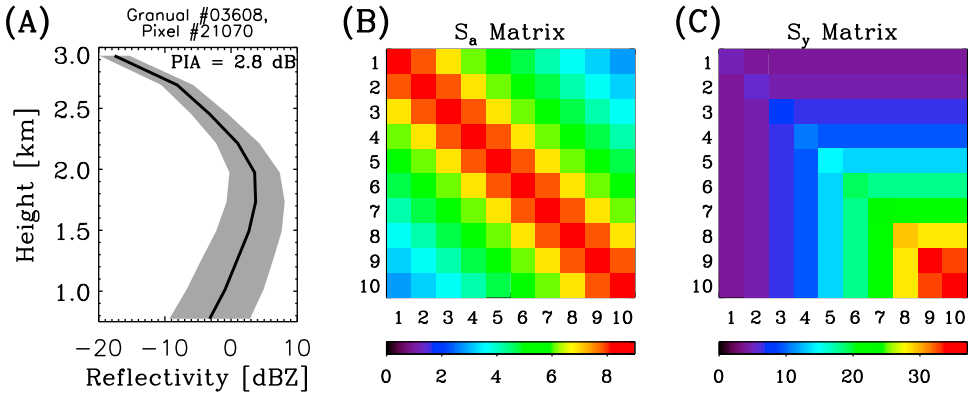

Figure 4. (a) A sample reflectivity profile with gray shading indicating the estimated observational uncertainty ($\sqrt{\mathbf{S}_{\mathbf{z},ii}}$). Also shown are the associated (b) $\mathbf{S_a}$ and (c) $\mathbf{S_z}$ error covariance matrices.

correlations between radar bins is set through the use of a correlation length scale (L) that allows the correlation to fall off as the distance between radar bins increases,

$$\rho_{ij} = \exp\left(\frac{-|z_i - z_j|}{L}\right). \quad (9)$$

The length scale should increase with the magnitude of the rain rate, which to first order can be estimated by the PIA [*Haynes et al.*, 2009]. To accomplish this effect a simple formulation is used here to define the length scale as $L = \Delta z(1 + \mathrm{PIA}^2)$, where Δz is the thickness of the radar range bins and PIA is expressed in dB. A minimum allowable value of Δz is imposed on the correlation length scale thus avoiding the problem of nonphysical negative length scales. This use of $\mathbf{S_a}$ as a smoothing constraint minimizes the possibility of the retrieved state containing unphysical oscillations in the vertical profile of rain when the rain becomes moderate to heavy in intensity. The precise formulation of the correlation length scale can be used as a tuning function to provide stability to the minimization while strengthening the integral constraint.

[27] The $\mathbf{S_z}$ measurement error covariance matrix is a function of both the measurement uncertainties (σ_{meas}), which are well characterized and the radiative transfer and physical model assumptions (σ_{mod}) which are much more difficult to quantify. In practice the uncertainty due to the model assumptions are larger and much more difficult to characterize than those associated with measurement uncertainty. The model assumptions that are critical in defining σ_{mod} are those which affect the Z-R relationship (σ_z) and those that affect the vertical distribution of attenuation (σ_{att}). The σ_{att} term describes the effect of a propagation of errors incurred in bins at the top of the profile to bins further from the radar as was described by *Hitschfeld and Bordan* [1954]. For example, the attenuation of the beam before reaching the first cloudy bin is negligible, however the attenuation-corrected reflectivity in bin 2 is a function of the assumptions made regarding bin 1 and so on along the radar path.

[28] Following from the above discussion, the diagonal elements of $\mathbf{S_z}$ are defined as $\mathbf{S}_{\mathbf{z},ii} = \sigma^2_{meas} + \sigma^2_z + \sigma^2_{att}$. The measurement uncertainty is well characterized and assigned the constant value of 1 dBZ [*Tanelli et al.*, 2008], which corresponds to a rain rate uncertainty that varies between 20% and 35% on the range 0.01 to 1 mm h^{-1}. The dominant assumption that determines forward model errors is that of the DSD and this uncertainty is estimated by taking the difference between the nimbostratus and cumulus congestus size distributions as the range of natural variability in the DSD. These quantities are assigned constant values of $\sigma_z = 2$ dB and $\sigma_{att} = 20\%$ based the relationships shown in Figure 2. The σ_z term has a constant value throughout the profile whereas the σ_{att} term is assigned a value of 20% of the total attenuation that is modeled between each bin and the radar. The σ_{att} term thus has the desired effect of increasing with depth into the profile, which tends to deweight reflectivities closer to the surface relative to reflectivity at cloud top. More complicated methods could be constructed to more precisely estimate the forward model uncertainties however it is our judgment that any additional level of complexity would be unjustified by our extremely limited a priori knowledge of the natural variability in the DSD.

[29] Off-diagonal elements of the $\mathbf{S_z}$ matrix are assigned using the formulation $\mathbf{S}_{\mathbf{z},ij} = \sigma^2_z + \min(\sigma^2_{att,ii}, \sigma^2_{att,jj})$. These elements represent the shared error variance between radar bins. Note that this value is always less than $\sqrt{\mathbf{S}_{\mathbf{z},ii}\mathbf{S}_{\mathbf{z},jj}}$ guarantying a physically plausible correlation less than unity. Thus reflectivity error is assumed to be perfectly correlated throughout the profile, whereas only the component of σ_{att} that is located physically above both radar bins is included in the off-diagonal elements. This formulation also assumes that σ_{meas} is uncorrelated between bins, which is approximately true although the oversampling of the CloudSat radar data introduces some correlations between adjacent 240 m bins.

[30] Uncertainty in the PIA is derived as a function of wind speed and sea surface temperature in the 2C-PRECIP-COLUMN product. Typically this value is on the order of 1 or 2 dB, however in extremely light wind situations it may be significantly larger. The total error in PIA also includes a term owing to errors in simulating it from the cloud and rainwater paths. Therefore, the total error variance in the PIA observation is $\sigma^2_{\mathrm{PIA}} = \sigma^2_{att} + \sigma^2_{meas}$ where σ_{att} is assigned as described above. Finally, uncertainty in τ is taken directly from the MOD06 product with a minimum allowable value of 25%.

[31] The details of the error characterization are important in two regards. First, the retrieval uncertainty that is derived from the OE method is a strong function of both $\mathbf{S_a}$ and $\mathbf{S_z}$

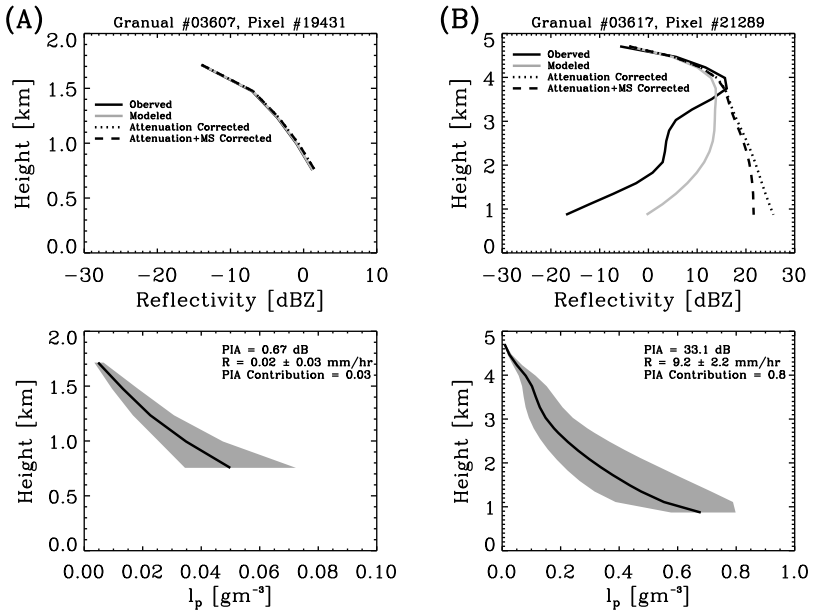

Figure 5. An example of (a) a light rain retrieval and (b) a heavy rain retrieval. (top) The observed and modeled reflectivity profiles as well as the modeled profile corrected for attenuation and multiple scattering. Not all lines are visible in Figure 5a (top) because they lie on top of each other. (bottom) The retrieved precipitation liquid water content (l_p) and associated 1σ uncertainty estimate (gray shading). The observed PIA, surface rain rate (R), and PIA contribution to the solution are shown.

necessitating realistic observation errors that account for both the relatively small measurement error and the much larger model assumption errors. Second, accounting for a state-dependent error estimate permits the same retrieval framework to seamlessly transition from a solution that is driven primarily by the reflectivity measurements to one that is driven primarily by the PIA. This seamless transition is made possible through the inclusion of correlations in $\mathbf{S_a}$ and $\mathbf{S_z}$ and the increasing value of σ_{att} with depth, which act to reduce the effective number of degrees of freedom of the reflectivity observations to some value less than N. Figure 4 shows a graphical depiction of the $\mathbf{S_a}$ and $\mathbf{S_z}$ matrices for a lightly precipitating cloud. This example illustrates that even in this relatively weakly attenuating case, strong correlations are imposed in $\mathbf{S_a}$ imposing a smoothing on the derived solution. The effect of increasing error variance with depth in $\mathbf{S_z}$ is also clearly evident illustrating another influence of the error characterization on the transition from a reflectivity-based to an attenuation-based solution.

4. Results and Discussion

4.1. Algorithm Mechanics

[32] The premise of the retrieval algorithm is that it gradually transitions from a reflectivity-driven solution to an attenuation-driven solution as the rain rate increases. Figure 5 shows two specific example retrievals to contrast the retrieval behavior in a light rain and a heavy rain event. In the light rain event the PIA is small and it is evident that the derived profiles of precipitation water content are being driven by the reflectivity profile because the derived reflectivity profiles match the observed profiles nearly exactly. In contrast, the attenuation is extreme in the heavy rain event and the retrieval is strongly influenced by the attenuation and smoothing constraints. While the retrieval matches the observed PIA well, the derived reflectivity profile shows significant deviation from the observed profile and the magnitude of this deviation increases with depth as was intended by the uncertainty characterization described in section 3.5. This case also clearly demonstrates the importance of multiple scattering in heavy precipitation where the modeled multiple-scattering correction to the observed reflectivities approaches 5 dBZ near the surface. To demonstrate that the behavior shown in Figure 5 is typical of the data set as a whole, a statistical comparison of the observed near-surface reflectivity and PIA with the retrieved rain rates is shown in

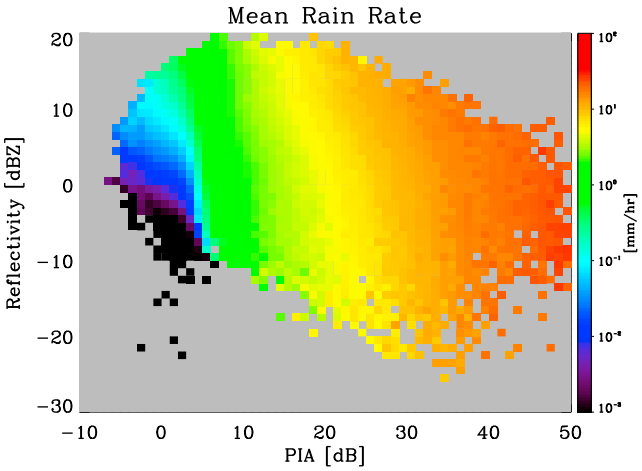

Figure 6. The relationship between the mean retrieved rain rate and the observed PIA and near-surface reflectivity. The observations are not corrected for attenuation or multiple scattering.

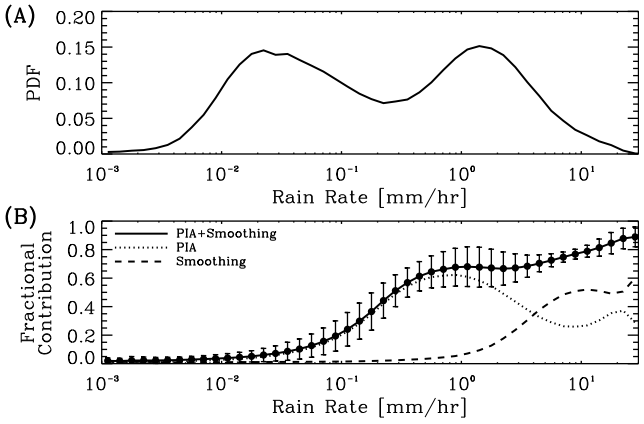

Figure 7. (a) The probability distribution function (PDF) of retrieved rain rates and (b) the mean fractional contribution of the attenuation constraint and the a priori smoothing constraint. The error bars show the standard deviation.

Figure 6, which reiterates that the derived rain rate is primarily a function of the reflectivity when the attenuation is low and transitions to an attenuation solution within the range of 0.1–0.5 mm h^{-1}.

[33] We turn now to a discussion of the distribution of the retrieved rain rates in shown in Figure 7a. The dynamic range of the rain rates exceeds four orders of magnitude from 0.001 mm h^{-1} to 30 mm h^{-1} with a mean of 1.18 mm h^{-1}. The results illustrate that light rain <1 mm h^{-1} account for 69.6% of the warm rain occurrence and 15.3% of the warm rain accumulation highlighting the importance of CloudSat as a complementary precipitation sensor to the TRMM PR. The bimodality of the distribution of rain rates in Figure 7a also requires some discussion. The bimodal peaks are indicative of the retrieval transitioning from a reflectivity mode to an attenuation mode as intended. The extent to which the transition from a reflectivity-driven to an attenuation-driven solution occurs can be quantified using the contribution matrices described in section 3.3. The PIA is used as a constraint both through the explicit constraint term and through the a priori smoothing term in equation (3), therefore the total contribution of PIA to the derived solution is taken as the sum of the PIA and the a priori contributions in equation (5). The effect of these two constraints is quantified in Figure 7b, which demonstrates that the total PIA contribution to the solution increases monotonically with rain rate with the most rapid transition occurring between 0.1 and 0.5 mm h^{-1}. Figure 7b further highlights that both the explicit PIA constraint and the a priori smoothing constraint contribute appreciably to the derived solution.

[34] While a rain rate bimodality may exist in nature, neither the reflectivities nor the PIA observations demonstrate two modes (see Figure 1), therefore the presence of this incongruity between the reflectivity and attenuation solutions suggests a potential bias in either the algorithm assumptions or the observations. The most likely algorithm assumption that could create this bias is that of the precipitation DSD, and the most likely observation that could create this bias is the PIA because the estimation of PIA requires imprecise and potentially biased ancillary knowledge of the 10 m wind speed and column integrated water vapor [*Lebsock et al.*, 2011]. If biases in the PIA could be mitigated, the incongruous bimodal character of the distribution suggests the possibility that a column-integrated parameter of the drop size distribution (i.e., the intercept parameter, N_o) could be retrieved.

[35] A characterization of the retrieval uncertainty calculated from the $\mathbf{S_x}$ error covariance matrix defined in equation (4) is provided in Figure 8 in which two distinct regimes are evident. For light rain rates where results are driven by the reflectivity profile, the retrieval uncertainty is on the order of 150%. As the rain rates exceed 0.5 mm h^{-1} and transition to an attenuation-based solution, the fractional uncertainty begins to decrease monotonically toward an asymptotic value near 40%. It must be noted that this uncertainty characterization does not include an estimate of multiple-scattering uncertainty, which should tend to increase with PIA and offset the monotonic decrease of uncertainty in the attenuation-driven regime.

4.2. Multiple Scattering

[36] Even in the warm rain examined here multiple-scattering effects on the CPR reflectivities are not negligible. Figure 9 demonstrates that while multiple-scattering effects exceeding a few dBZ are relatively rare, these cases account for a disproportionately large fraction of the total rain accumulation. For example only 8.6% of warm rain has a surface multiple-scattering signal that exceeds 2 dBZ, however these cases account for 50.7% of the warm rain accumulation. To test the sensitivity of the retrieval to multiple-scattering effects the retrieval was rerun with the multiple-scattering correction turned off which will have the effect of decreasing Z_{sim} profiles and increasing PIA_{sim}. Figure 10 shows that the resultant effect is to decrease the heavy rain rates, due to the dominance of the PIA constraint in heavy rain. This causes an underestimation of the mean rain rate of −24.4%. The multiple-scattering correction is very sensitive to the assumed DSD because of the manner in which the attenuation and

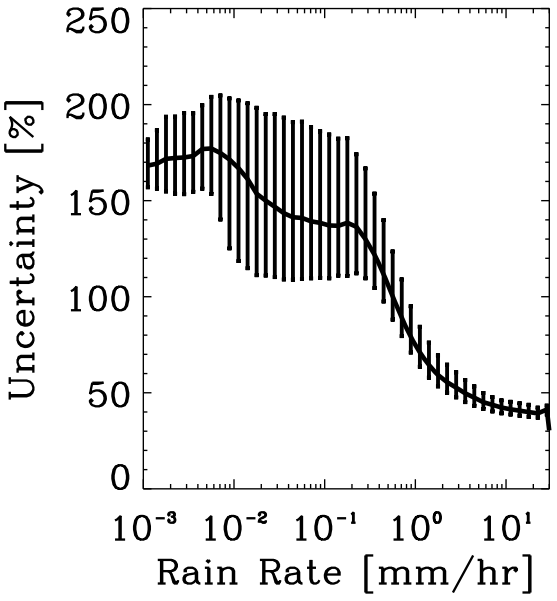

Figure 8. The median 1σ uncertainty estimate in the surface rain rate. The error bars cover a range that spans 75% of the data.

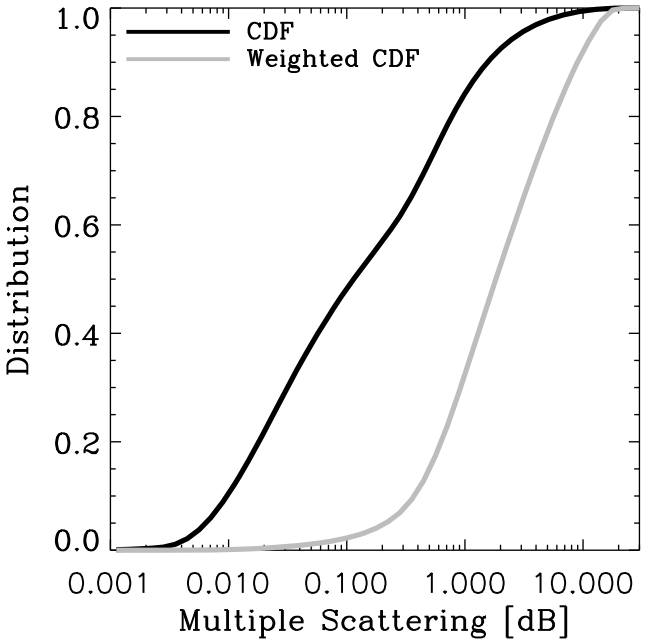

Figure 9. The cumulative distribution function (CDF) of the multiple-scattering correction at the surface (black). The weighted CDF (gray) is weighted by rain rate and is therefore representative of the total rainfall accumulation.

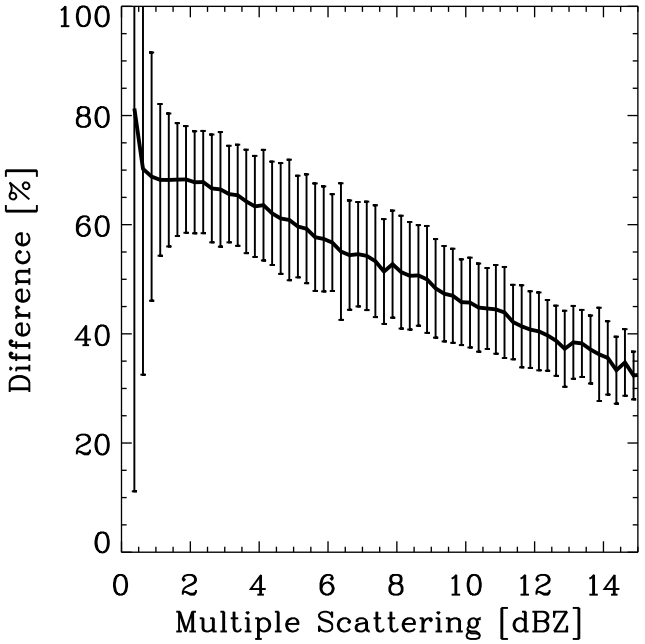

Figure 11. The difference between the surface multiple-scattering correction from a test in which a Marshall-Palmer size distribution is assumed and the standard retrieval. Note that the difference equals Marshall-Palmer minus standard, so that the multiple scattering of the Marshall-Palmer DSD is seen to overestimate that of the warm rain DSD.

scattering phase function vary with DSD. In particular, DSDs composed of large drops tend to have more forward scattering than DSDs composed of small drops, which tend to scatter more isotropically. Figure 11 shows that when the warm rain DSD is replaced with a Marshall-Palmer distribution the multiple-scattering signal increases by up to 100%. Therefore errors in the multiple scattering are dominated by DSD assumptions and increasing the accuracy of the radar model by incorporating a more complex and computationally demanding multiple-scattering model than the TDTS model is not justified. Furthermore, while the error characterization shown in Figure 8 does not account for multiple-scattering contributions to retrieval error, due to the sensitivity of the multiple scattering to the DSD, rainfall retrievals with multiple-scattering corrections exceeding ~5 dB warrant an additional degree of scrutiny. 2.6% of the warm rain retrievals considered here exceed this threshold. In the 2C-RAIN-PROFILE product these pixels will be flagged as questionable in a retrieval confidence flag included in the product file.

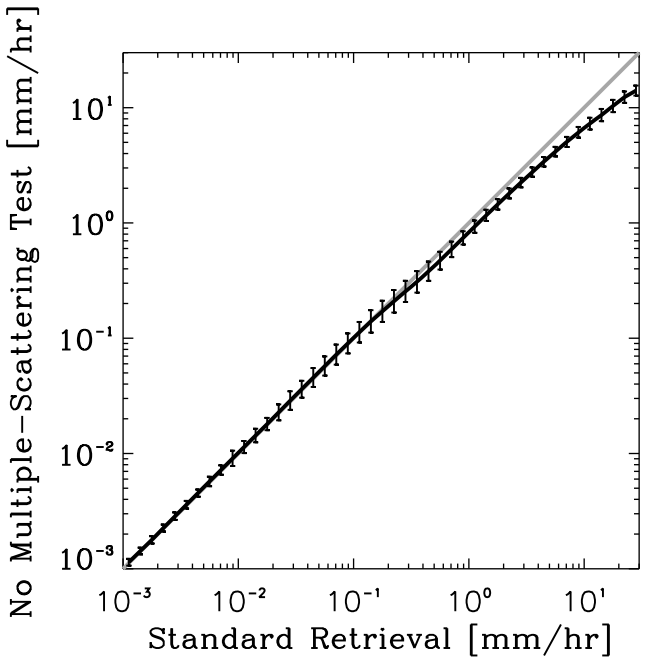

Figure 10. A comparison of the standard retrieval and a test in which multiple scattering is not modeled. The black line shows the mean, and the error bars show the standard deviation.

4.3. Drop Size Distribution

[37] The Marshall-Palmer DSD used in previous implementations of this algorithm is simply inappropriate for warm rain events. Figure 12 highlights the impact of assuming a Marshall-Palmer DSD on the retrieved rain rates. The Marshall-Palmer DSD tends to underestimate rain rates in the reflectivity regime and overestimate rain rates in the attenuation regime. This result is quite consistent with the optical properties provided in Figure 2, which show that for a given rain rate, the warm rain DSDs have more water and larger number concentrations than the Marshall-Palmer DSD resulting in smaller reflectivities and larger attenuations. Although there are compensating errors at the light and heavy end of the spectrum, mean rain rates overestimated by a factor of two when a Marshall-Palmer DSD is assumed because the total accumulation is weighted strongly toward the heavy rain events.

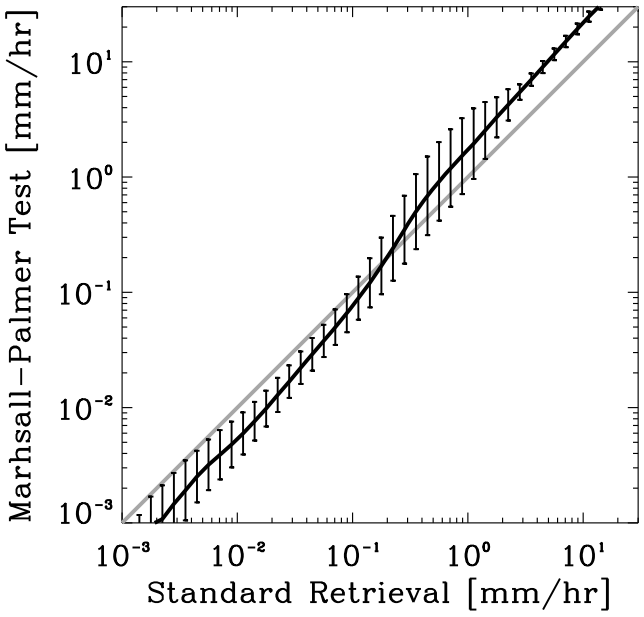

Figure 12. A comparison of the standard retrieval and a test in which a Marshall-Palmer DSD is assumed. The black line shows the mean, and the error bars show the standard deviation.

4.4. Evaporation

[38] A novel element of this retrieval is the modeling of evaporation of light rain and drizzle below cloud base. To quantify the effect of the evaporation parameterization on the derived rain rates, the algorithm was tested with the evaporation model disabled. Results are presented in Figure 13, which demonstrates that the evaporation model tends to reduce the rain rate in weakly precipitating clouds with little noticeable change above 1 mm h^{-1}. The difference in the mean rain rate is only 13.2%, however this difference is likely to be significantly more pronounced on regional scales in regimes that are dominated by weakly precipitating stratocumulus.

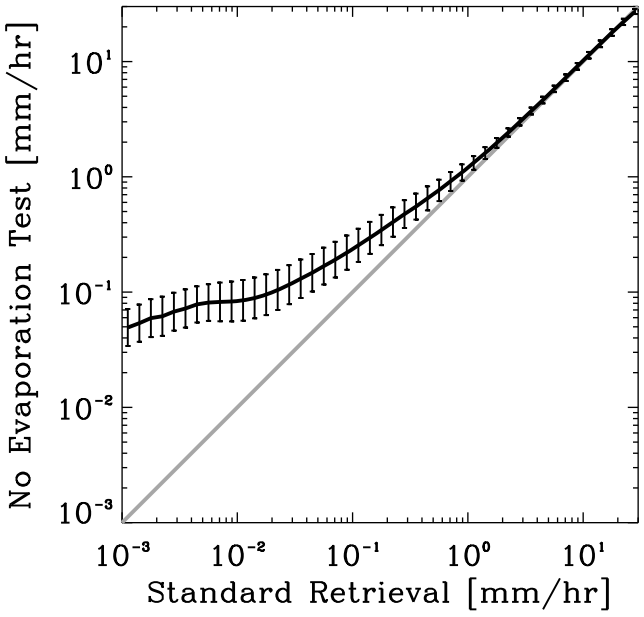

Figure 13. A comparison of the standard retrieval against a test in which the subcloud evaporation is disabled. The solid black line shows the mean, and the error bars show the standard deviations.

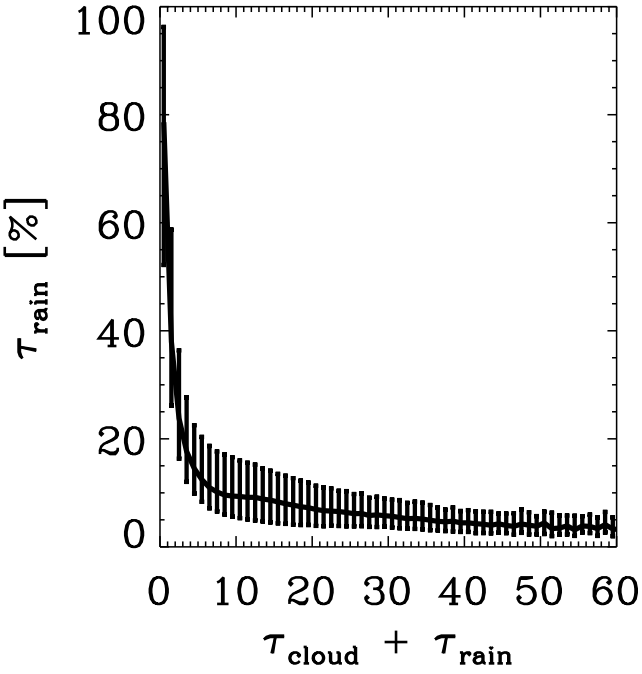

Figure 14. The modeled rain visible optical depth (τ_{rain}) as a function of the total modeled optical depth ($\tau_{cloud} + \tau_{rain}$). The error bars cover a range that spans 75% of the data.

4.5. Cloud Water

[39] MODIS observations of the visible optical depth were included in this retrieval in an effort to constrain the cloud water path, which has a negligible effect on the reflectivities but can account for an appreciable fraction of the attenuation in light rain. Instead of simply assigning a MODIS water path for each retrieval, W_c was included as a retrieval parameter to account for the effect of precipitation water on the observed visible optical depth. Figure 14 demonstrates that the effect of precipitation water on the optical depth is roughly on the order of 10%, implying a 10% difference in the cloud component of the attenuation from that which would be assigned by assuming that the optical depth is purely a function of cloud water.

[40] The visible optical depth observation is only available during daylight hours, therefore the cloud water path must be assumed at night. This is particularly relevant for the 2C-RAIN-PROFILE product that to date has neglected the presence of cloud water. To this end, a simple least squares approach is used to develop a parameterization of the cloud water path given the cloud height and surface rain rate,

$$\begin{aligned} \log_{10}(W_c) &= 2.147 + 0.011H + 0.132\log_{10}(R): \quad \text{Nimbostratus} \\ \log_{10}(W_c) &= 2.186 + 0.017H + 0.129\log_{10}(R): \quad \text{Congestus} \end{aligned}, \tag{10}$$

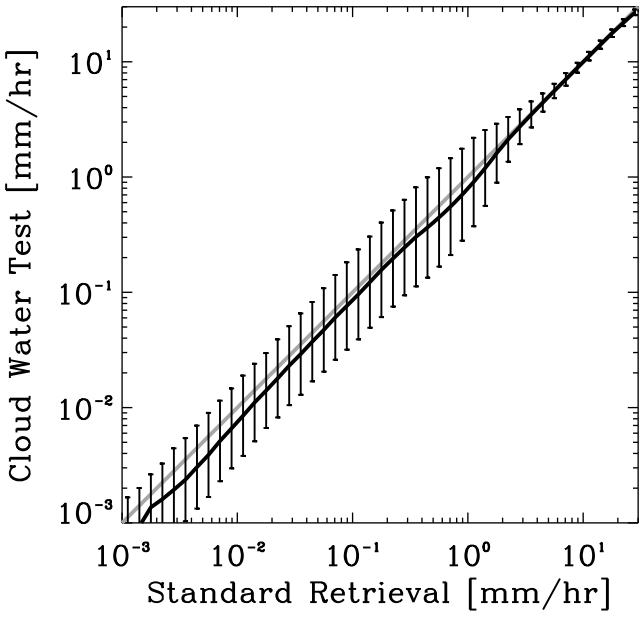

Figure 15. A comparison of the standard retrieval against a test in cloud water is parameterized using equation (10). The solid black line shows the mean, and the error bars show the standard deviations.

with W_c expressed in gm^{-2}, H in km and R in mm h^{-1}. We note that a tremendous amount of natural variability exists in the cloud water path and therefore the parameterized W_c correlates relatively poorly with the observed W_c ($\rho = 0.39$). Nonetheless this parameterization captures some gross features of the cloud water path that provides a basis for ascribing cloud water when ancillary visible optical depth observations are unavailable. Figure 15 shows a comparison of the standard retrieval with one in which the visible optical depth constraint in equation (3) is removed and cloud water is assigned using equation (10). The difference in the mean rain rates is less than 1% with the largest differences not exceeding 5% occurring at light rain rates. These errors are clearly small relative to the more critical assumptions, especially that of the rain DSD justifying the use of equation (10) in the operational 2C-RAIN-PROFILE CloudSat algorithm.

4.6. Comparison to the 2C-PRECIP-COLUMN Product

[41] The attenuation-based 2C-PRECIP-COLUMN [*Haynes et al.*, 2009] rainfall product has existed prior to the development of this algorithm and is beginning to be used by the scientific community [e.g., *Berg et al.*, 2010; *Stephens et al.*, 2010] for quantitative purposes. Therefore, it is of some interest to compare the rain rates presented here with the 2C-PRECIP-COLUMN results. 2C-PRECIP-COLUMN has some similarities with the current retrieval, for example the effects of multiple scattering on the PIA have been accounted for and a parameterization of the water path derived using MODIS data has been included in the algorithm, however notable differences exist including the assumption of a Marshall-Palmer DSD and the assumption that the rain column is vertically uniform. Of particular importance, the assumption of a vertically invariant rain column causes 2C-PRECIP-COLUMN to be a better indicator of the integrated rainwater path than the surface rain rate. These algorithm assumptions are tailored toward tropical stratiform precipitation and are not well suited to warm rain, however the manner in which they will affect the retrieval is not immediately evident.

[42] Figure 16 shows that the 2C-PRECIP-COLUMN product tends to underestimate heavy precipitation and overestimate light precipitation with respect to the current work. These differences are opposite those that one would expect from the assumption of a Marshall-Palmer DSD (e.g., Figure 12). Instead the differences are largely attributable to the assumption of a vertically invariant rain column. For example, 2C-PRECIP-COLUMN does not account for the evaporation process, which results in a systematic vertical distribution in the rainwater mass that causes that product to overestimate light rain rates. Evaporation is negligible in heavy rain, but in these cases rainwater content tends to increase with depth into the cloud and maximize near cloud base causing the 2C-PRECIP-COLUMN to systematically overestimate the depth of the rain column and thus underestimate the surface rain rate. Partly due to a fortuitous cancellation of errors at the low and high rain rates, the 2C-PRECIP-COLUMN is only 52% lower than the retrieval presented here.

[43] Based on the results of this work, future releases of the 2C-PRECIP-COLUMN will attempt to address the systematic overestimation of the depth of the rain column. However, given the notable differences between the two algorithms we recommend caution in the interpretation of the 2C-PRECIP-COLUMN rain rates when applied to warm rain events. We emphasize that the 2C-PRECIP-COLUMN product is primarily intended as a flagging product that should be used to identify the occurrence of rain whereas the algorithm

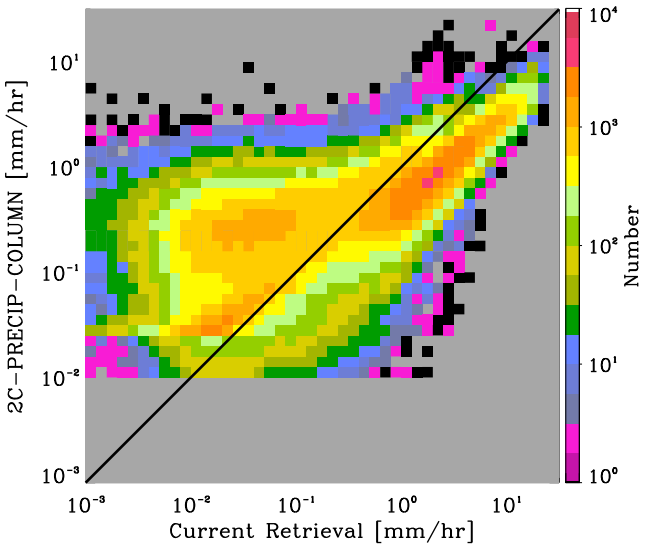

Figure 16. The joint histogram of the estimated surface rain rate from the current retrieval and the 2C-PRECIP-COLUMN (R04) product.

presented here, which forms the basis of the 2C-RAIN-PROFILE product, is favored for quantitative purposes.

5. Conclusions

[44] Early results from CloudSat demonstrate the ubiquity of warm rain over the oceans that is not captured by other satellite sensors. To date, efforts to quantify this rain have been hindered by rainfall retrieval algorithms that are not specifically tailored to warm rain. To address this shortcoming we have presented an algorithm for the retrieval of warm rain from CloudSat and MODIS observations that builds upon the work of *L'Ecuyer and Stephens* [2002], which forms the basis of the standard CloudSat 2C-RAIN-PROFILE product. The premise of the algorithm is that it smoothly transitions from a reflectivity-driven solution at light rain rates to an attenuation-driven solution at moderate and heavy rain rates through the use of an integral constraint on the path integrated attenuation, thus harnessing the noise of attenuation as an exploitable signal and significantly extending the useful range of CloudSat as a precipitation sensor.

[45] A rigorous characterization of measurement and algorithm assumption uncertainties as well as the correlation of assumption errors between radar range gates is outlined in this paper. This error characterization serves two important purposes. It determines the character of the transition from a reflectivity-driven retrieval to an attenuation-driven retrieval through a relative weighting of the attenuation and the reflectivity observations and it provides a conservative retrieval uncertainty estimate. A quantitative analysis of the algorithm mechanics demonstrates that the retrieval transitions between the reflectivity and attenuation modes within the range of 0.1–0.5 mm h^{-1}. At low rain rates the retrieval uncertainty is dominated by the reflectivity observations and is estimated at 150% while at higher rain rates the retrieval uncertainty is dominated by the PIA and decreases monotonically to a value of 40%. These relatively large uncertainty estimates represent the random component of the error, which can be reduced through adequate sampling, however we emphasize that they do not address the more difficult issue of biases that may remain due to regime-dependent algorithm assumptions [e.g., *Berg et al.*, 2006].

[46] The flexibility of the optimal estimation retrieval framework used by the 2C-RAIN-PROFILE algorithm is used here to implement several physical models. For example, the visible optical depth is used as an additional integral constraint on the cloud component of the total water path, eliminating a critical assumption in the retrieval of light rain. The standard retrieval with the optical depth constraint is used to construct a parameterization of the cloud water path that can be exploited at night when visible optical depth observations are unavailable. Tests of the retrieval with the cloud water parameterization (no optical depth constraint) against the standard retrieval (with optical depth constraint) show differences less than 1% in the mean retrievals, indicating that the cloud water parameterization is sufficiently accurate for implementation in the 2C-RAIN-PROFILE algorithm. Another element of this work specific to the retrieval of warm rain is a representation of the precipitation DSD appropriate for warm rain. Comparison of the standard retrieval against a retrieval using a Marshall-Palmer DSD show that the Marshall-Palmer assumption overestimates the mean rain rate by a factor of 2 and distorts the character of rain by widening the distribution of derived rain rates. A model of evaporation below cloud base that tends to reduce the surface rain rate has also been included in the algorithm. Results suggest that neglecting subcloud evaporation causes a 13% high bias in the mean warm rain rate, and that most of this bias derives from rain rates below 1 mm h^{-1}. This result could have significant regional implications in regimes where the dominant mode of precipitation is that of drizzle falling from stratocumulus. A more general enhancement of the retrieval architecture is the implementation of fast multiple-scattering radar model. This model is used to show that even in the warm rain examined here, neglecting multiple scattering can result in a bias of −24.4% in the mean rain rate. The model is further used to show that the modeled multiple scattering is so sensitive to the assumed DSD that use of a more accurate model of multiple scattering is unjustified.

[47] Because of its unique sensitivity to light rain, CloudSat adds significantly to our understanding of the global hydrologic cycle. In particular it provides a rich view of warm rain processes that are largely missed by conventional satellite remote sensing. The algorithm developments reported here are motivated by a desire to better quantify this missing rain and form the basis of ongoing improvements to the operational 2C-RAIN-PROFILE product. With these modifications the 2C-RAIN-PROFILE product will provide a complimentary view of global scale warm rain to that of the TRMM PR [i.e., *Kodama et al.*, 2009; *Liu and Zipser*, 2009], ahead of future missions such as the Global Precipitation Measurement Mission and the Aerosol/Cloud/Ecosystems Mission both of which are scoped to fly dual wavelength high-frequency radar systems.

[48] **Acknowledgments.** This study was supported by NASA CloudSat/CALIPSO science team research grant NNX10AM29G.

References

Arkin, P. A. (1979), The relationship between fractional coverage of high cloud and rainfall accumulations during GATE over the B-scale array, *Mon. Weather Rev.*, *107*, 1382–1387, doi:10.1175/1520-0493(1979)107<1382:TRBFCO>2.0.CO;2.

Battaglia, A., J. M. Haynes, T. L'Ecuyer, and C. Simmer (2008), Identifying multiple-scattering-affected profiles in CloudSat observations over the oceans, *J. Geophys. Res.*, *113*, D00A17, doi:10.1029/2008JD009960.

Battan, L. J., and R. R. Braham Jr. (1956), A study of convective precipitation based on cloud and radar observations, *J. Meteorol.*, *13*, 587–591, doi:10.1175/1520-0469(1956)013<0587:ASOCPB>2.0.CO;2.

Bennartz, R. (2007), Global assessment of marine boundary layer cloud droplet number concentration from satellite, *J. Geophys. Res.*, *112*, D02201, doi:10.1029/2006JD007547.

Berg, W., T. L'Ecuyer, and C. Kummerow (2006), Rainfall climate regimes: The relationship of regional TRMM rainfall biases to the environment, *J. Appl. Meteorol. Climatol.*, *45*, 434–454, doi:10.1175/JAM2331.1.

Berg, W., T. L'Ecuyer, and J. M. Haynes (2010), The distribution of rainfall over oceans from spaceborne radars, *J. Appl. Meteorol. Climatol.*, *49*, 535–543, doi:10.1175/2009JAMC2330.1.

Chen, R., Z. Li, R. Kuligowski, R. Ferraro, and F. Wang (2011), A study of warm rain detection using A-Train satellite data, *Geophys. Res. Lett.*, *38*, L04804, doi:10.1029/2010GL046217.

Comstock, K. K., R. Wood, S. E. Yuter, and C. S. Bretherton (2004), Reflectivity and rain rate in and below drizzling stratocumulus, *Q. J. R. Meteorol. Soc.*, *130*, 2891–2918, doi:10.1256/qj.03.187.

Gunn, R., and G. D. Kinzer (1949), The terminal velocity of fall for water droplets in stagnant air, *J. Atmos. Sci.*, *6*, 243–248.

Haynes, J. M., T. S. L'Ecuyer, G. L. Stephens, S. D. Miller, C. Mitrescu, N. B. Wood, and S. Tanelli (2009), Rainfall retrieval over the ocean with spaceborne W-band radar, *J. Geophys. Res.*, *114*, D00A22, doi:10.1029/2008JD009973.

Hitschfeld, W., and J. Bordan (1954), Errors inherent in the radar measurement of rainfall at attenuating wavelengths, *J. Meteorol.*, *11*, 58–67, doi:10.1175/1520-0469(1954)011<0058:EIITRM>2.0.CO;2.

Hogan, R. J., and A. Battaglia (2008), Fast lidar and radar multiple-scattering models, Part II: Wide-angle scattering using the time-dependent two-stream approximation, *J. Atmos. Sci.*, *65*, 3636–3651, doi:10.1175/2008JAS2643.1.

Iguchi, T., T. Kozu, R. Meneghini, J. Awaka, and K. Okamoto (2000), Rain-profiling algorithm for the TRMM precipitation radar, *J. Appl. Meteorol.*, *39*, 2038–2052, doi:10.1175/1520-0450(2001)040<2038:RPAFTT>2.0.CO;2.

Kodama, Y.-M., M. Katsumata, S. Mori, S. Satoh, Y. Hirose, and H. Ueda (2009), Climatology of warm rain and associated latent heating derived from TRMM PR observations, *J. Clim.*, *22*, 4908–4929, doi:10.1175/2009JCLI2575.1.

Kummerow, C. D., S. Ringerud, J. Crook, D. Randel, and W. Berg (2011), An observationally generated a priori database for microwave rainfall retrievals, *J. Atmos. Oceanic Technol.*, *28*, 113–130, doi:10.1175/2010JTECHA1468.1.

Lebsock, M. D., G. L. Stephens, and C. Kummerow (2008), Multisensor satellite observations of aerosol effects on warm clouds, *J. Geophys. Res.*, *113*, D15205, doi:10.1029/2008JD009876.

Lebsock, M. D., T. S. L'Ecuyer, and G. L. Stephens (2011), Detecting the ratio of rain and cloud water in low-latitude shallow marine clouds, *J. Appl. Meteorol. Climatol.*, *50*, 419–432, doi:10.1175/2010JAMC2494.1.

L'Ecuyer, T. S., and G. L. Stephens (2002), An estimation-based precipitation retrieval algorithm for attenuating radars, *J. Appl. Meteorol.*, *41*, 272–285, doi:10.1175/1520-0450(2002)041<0272:AEBPRA>2.0.CO;2.

Leon, D. C., Z. Wang, and D. Liu (2008), Climatology of drizzle in marine boundary layer clouds based on 1 year of data from CloudSat and Cloud-Aerosol Lidar and Infrared Pathfinder Satellite Observations (CALIPSO), *J. Geophys. Res.*, *113*, D00A14, doi:10.1029/2008JD009835.

Liu, C., and E. J. Zipser (2009), "Warm rain" in the tropics: Seasonal and regional distributions based on 9 yr of TRMM data, *J. Clim.*, *22*, 767–779, doi:10.1175/2008JCLI2641.1.

Lovejoy, S., and G. L. Austin (1979), The delineation of rain areas from visible and IR satellite data for GATE and mid-latitudes, *Atmos. Ocean*, *17*, 77–92, doi:10.1080/07055900.1979.9649053.

Marchand, R., G. G. Mace, T. Ackerman, and G. Stephens (2008), Hydrometeor detection using Cloudsat—An Earth-orbiting 94-GHz cloud radar, *J. Atmos. Oceanic Technol.*, *25*, 519–533, doi:10.1175/2007JTECHA1006.1.

Marshak, A., S. Platnick, T. Várnai, G. Wen, and R. F. Cahalan (2006), Impact of three-dimensional radiative effects on satellite retrievals of cloud droplet sizes, *J. Geophys. Res.*, *111*, D09207, doi:10.1029/2005JD006686.

Marshall, J. S., and W. M. Palmer (1948), The distribution of raindrops with size, *J. Meteorol. 5*, 165–166, doi:10.1175/1520-0469(1948)005<0165:TDORWS>2.0.CO;2.

Matrosov, S. Y. (2007), Potential for attenuation-based estimations of rainfall rate from CloudSat, *Geophys. Res. Lett.*, *34*, L05817, doi:10.1029/2006GL029161.

Mitrescu, C., T. L'Ecuyer, J. Haynes, S. Miller, and J. Turk (2010), CloudSat precipitation profiling algorithm-model description, *J. Appl. Meteorol. Climatol.*, *49*, 991–1003, doi:10.1175/2009JAMC2181.1.

Nakajima, T., and M. D. King (1990), Determination of the optical thickness and effective particle radius of clouds from reflected solar radiation measurements, Part I: Theory, *J. Atmos. Sci.*, *47*, 1878–1893, doi:10.1175/1520-0469(1990)047<1878:DOTOTA>2.0.CO;2.

Petty, G. (1995), Frequencies and characteristics of global oceanic precipitation from shipboard present-weather reports, *Bull. Am. Meteorol. Soc.*, *76*, 1593–1616, doi:10.1175/1520-0477(1995)076<1593:FACOGO>2.0.CO;2.

Platnick, S. (2000), Vertical photon transport in cloud remote sensing problems, *J. Geophys. Res.*, *105*(D18), 22,919–22,935, doi:10.1029/2000JD900333.

Platnick, S., M. D. King, S. A. Ackerman, W. P. Menzel, B. A. Baum, J. C. Riedi, and R. A. Frey (2003), The MODIS cloud products: Algorithms and examples from Terra, *IEEE Trans. Geosci. Remote Sens.*, *41*, 459–473, doi:10.1109/TGRS.2002.808301.

Schumacher, C., and R. A. Houze (2000), Comparison of radar data from the TRMM satellite and Kwajalein oceanic validation site, *J. Appl. Meteorol.*, *39*, 2151–2164, doi:10.1175/1520-0450(2001)040<2151:CORDFT>2.0.CO;2.

Short, D. A., and K. Nakamura (2000), TRMM radar observations of shallow precipitation over the tropical oceans, *J. Clim.*, *13*, 4107–4124, doi:10.1175/1520-0442(2000)013<4107:TROOSP>2.0.CO;2.

Snodgrass, E. R., L. Di Girolamo, and R. M. Rauber (2009), Precipitation characteristics of trade wind clouds during RICO derived from radar, satellite, and aircraft measurements, *J. Appl. Meteorol. Climatol.*, *48*, 464–483, doi:10.1175/2008JAMC1946.1.

Stephens, G. L. (1978), Radiation profiles in extended water clouds, Part II: Parameterization schemes, *J. Atmos. Sci.*, *35*, 2123–2132, doi:10.1175/1520-0469(1978)035<2123:RPIEWC>2.0.CO;2.

Stephens, G. L., and C. D. Kummerow (2007), The remote sensing of clouds and precipitation from space: A review, *J. Atmos. Sci.*, *64*, 3742–3765, doi:10.1175/2006JAS2375.1.

Stephens, G. L., T. L'Ecuyer, R. Forbes, A. Gettlemen, J.-C. Golaz, A. Bodas-Salcedo, K. Suzuki, P. Gabriel, and J. Haynes (2010), Dreary state of precipitation in global models, *J. Geophys. Res.*, *115*, D24211, doi:10.1029/2010JD014532.

Tanelli, S., S. L. Durden, E. Im, K. S. Pak, D. G. Reinke, P. Partain, J. M. Haynes, and R. T. Marchand (2008), CloudSat's cloud profiling radar after two years in orbit: Performance, calibration, and processing, *IEEE Trans. Geosci. Remote Sens.*, *46*, doi:10.1109/TGRS.2008.2002030.

Wilheit, T. T. (1986), Some comments on passive microwave measurement of rain, *Bull. Am. Meteorol. Soc.*, *67*, 1226–1232, doi:10.1175/1520-0477(1986)067<1226:SCOPMM>2.0.CO;2.

M. D. Lebsock and T. S. L'Ecuyer, Department of Atmospheric Science, Colorado State University, 200 W. Lake St., Fort Collins, CO 80523-1371, USA. (lebsock@atmos.colostate.edu)